Metals and Materials International (2023) 29:3423–3441
https://doi.org/10.1007/s12540-023-01462-2

Effect of in-Situ Intrinsic Heat Treatment in Metal Additive Manufacturing: A Comprehensive Review

Sivakumar Munusamy[1] · **J. Jerald**[1]

Received: 1 January 2023 / Accepted: 2 May 2023 / Published online: 26 May 2023
© The Author(s) under exclusive licence to The Korean Institute of Metals and Materials 2023

Abstract

Metal Additive Manufacturing (MAM) produces high-strength and complex shape components through a layer-by-layer metal deposition approach for aerospace, automobile, and structural applications. The heat is accumulated and subjected to reheating in the metal layers by depositing material from the feedstock with the help of a heat source on the existing metal layer. Generally, the reheating in the MAM process consists of multiple annealing, multilevel normalizing, and long tempering processes. The material morphology and mechanical properties of MAM products are affected due to the stored heat in the layers while the component is manufactured with the heat source of laser energy, electron energy, or conventional arc welding techniques. The grain structure is refined by reheating the layers by the heat source and without post-heat treatment techniques. The mechanical properties and morphological characteristics of the as-built MAM components due to the effect of in-situ intrinsic heat treatment (reheating) are measured through various materials testing methods such as Electron Back Scatter Diffraction (EBSD), Scanning electron microscopy (SEM), X-ray diffraction (XRD), tensile test, hardness test, compressive test and etc. The review aims to study the mechanical and morphological characteristics due to the effect of in-situ intrinsic heat treatments on low carbon steel, maraging steel, and Al alloys, which were fabricated by direct energy deposition (DED) and laser powder bed fusion (LPBF) techniques.

Keywords Metal additive manufacturing (MAM) · Laser powder bed fusion · Heat treatment · In-situ intrinsic heat treatment · Microstructures · Mechanical characteristics

Abbreviations

AF	Acicular ferrite
AM	Additive manufacturing
CAD	Computer-aided design
CGF	Coarse granular ferrite
CGHAZ	Coarse-grain heat-affected zone
CGZ	Columnar grain zone
DED	Direct energy deposition
EBM	Electron beam melting
EDS	Energy-dispersive x-ray spectroscopy
EBSD	Electron back scatter diffraction
FGF	Fine grain ferrite
FGHAZ	Fine grain heat-affected zone
GBF	Grain boundary ferrite
GMAW	Gas metal arc welding
GTAW	Gas tungsten arc welding
HIP	Hot isostatic pressing
HSLA	High-strength low-alloy
HT	Heat treatmen
HV	Vickers hardness
IHT	Intrinsic heat treatment
IPF	Inverse pole figures
ICFGHAZ	Inter-critically reheated FGHAZ
KAM	Kernel average misorientation
LAM	Laser additive manufacturing
L-DED	Laser direct energy deposition
LMD	Laser metal deposition
LP	Lamellar pearlite
MAM	Metal additive manufacturing
PAW	Plasma arc welding
PBF	Powder bed fusion
PF	Polygonal ferrite
PH	Post heat treatment
PRF	Partially refined ferrite
RH	Reheating
SAAM	Submerged arc additive manufacturing
SAXS	Small-angle x-ray scattering

✉ Sivakumar Munusamy
siva.sky06@gmail.com

[1] Department of Production Engineering, National Institute of Technology Tiruchirappalli, Tiruchirappalli, India

SCFGHAZ	Sub-critically reheated FGHAZ
SEM	Scanning electron microscopy
SRF	Stress-released ferrite
SLM	Selective laser melting
TEM	Transmission electron microscopy
UTS	Ultimate tensile strength
WAAM	Wire arc additive manufacturing
WAXS	Wide-angle x-ray scattering
XRD	X-ray diffraction

1 Introduction

The fabrication of complex-shaped with near-net-shape products is challenging when using traditional processes. In modern technology, these kinds of features are achieved by Additive Manufacturing (AM) methods such as Direct Energy Deposition (DED) and Powder Bed Fusion (PBF) additive manufacturing in various sectors [1], like aerospace [2], machinery [3], automobile [4], marine [5], and medical implants. Metal additive manufacturing (MAM) has grown dramatically with layer upon layer strategic approach due to low material waste, improved surface finish, and its ability to manufacture products with specific mechanical properties [6].

MAM is divided into two major categories such as PBF and DED based on the heat source, type of melting, and material feed (powder or wire) [7]. The importance and significance of a few metal AM technologies are explained in Sect. 2. Due to high solidification rate the Selective Laser Melting (SLM) produces complex shapes and high surface quality component. Wire arc additive manufacturing technology has a high deposition rate in the large-scale applications [8]. The WAAM method is unsatisfactory due to anisotropy issues in microstructure, residual stress, distortion, and poor surface finish [9].

Laser Metal Deposition (LMD) phases consist of three phases: During the LMD process, the small molten metal pool temperature and its heat transfer rate are more effective into the sublayers, and also the substrate receives a fast cooling rate during the solidification [10–13]. Second, as the laser travels through a previously deposited bulk volume during the formation of adjacent paths and consecutive layers, the metal is continuously heated and continuously reheated with a slowly reducing temperature. One such category of Intrinsic Heat Treatment (IHT) contains rapid temperature flowing up to closer melting temperatures [11, 14–16]. LMD products, in comparison to conventional manufacturing, provide a more complex thermal behavior [17]. Third, because of the metal-based LAM method, the chemical properties of materials could be tuned even during manufacturing by utilizing two or more powder feed and a powder mixing chamber before the feed intake nozzle. It poses good surface structure and properties by multiple heating and building up cooling to each constitutive layers [18]. Due to lower heat dissipation and sequential high-temperature cycles in MAM process, resulting in distortion and low surface finish. The processing parameters were optimized to avoid these defects [9].

Wang et al. [20] discussed precipitation formation of a ductile phase formation by IHT to improve toughness during post-weld heat treatment on HSLA steel. Dirisu et al. [19] the compressive stress caused by rolling on AM deposited material improved mild steel's mechanical and fatigue characteristics. Similarly, the microstructure optimization and mechanical properties of stainless steel were enhanced by hot forging. The effectiveness of hot forging on the AM components depends on the forging pressure and temperature [20].

Maraging steels are advanced high strength steels that integrate high mechanical properties such as high strengths with excellent tensile and flexural properties [21, 22]. Maraging steels are mostly used in aerospace, energy, and tooling industries [23–25]. These beneficial mechanical properties are due to a martensitic crystalline structure that has been formed by higher densities of interfacial precipitates obtained during tempering by IHT in the layer by layer fabrication technique [26, 27]. In the particular circumstance of the age of heat-treated aluminum alloys, the IHT effects cause rapid precipitates and grain refinement. Controlling these complex reactions requires understanding the microstructural evolution at various length scales [28].

Significant residual stresses were typically encountered in SLM components due to the high heating/cooling rates used in laser processing. Interlayer debonding and stress cracking might result from residual stress [29]. Tzu Hou Hsu et al. [30] studied the mechanical characteristics of SLM AM 17-4 PH SS after post-heat treatments. The residual stress was often achieved on top and bottom of the as-built SLM sample, with moderate compression stress at the huge intermediate zone. Preheat the building substrate to reduce the thermal gradient, which reduces the stress level [31]. Post-fabrication heat treatments can also remove or minimize residual stress [32, 33].

The material properties are generally enhanced by conventional post heat treatment techniques such as annealing, normalizing, hardening, and tempering. In the layer-by-layer deposition technique, the existing layer undergoes multiple reheating processes such as annealing, normalizing and followed by tempering process. The mechanical properties of metal AM components are enhanced by changing the microstructure due to reheating. This review aims to view the impact of intrinsic heat treatment on the material microstructure and mechanical properties of various AM materials such as low carbon steel, stainless steel, Aluminum alloys, Titanium alloys, etc.

2 Methods of Metal Additive Manufacturing

In metal AM, the feedstock material (powder or wire) is completely melted by the heat source and deposited on the substrate through layer by layer approach [38]. Metal powders are generally used in the common metal AM process instead of metal wires [39]. All metal AM processes are build the components through layer upon layer techniques; however, the most common methods of metal AM [40] are wire arc additive manufacturing (WAAM) [41], direct energy deposition (DED) [42, 43], sheet lamination [44], and laser powder bed fusion (LPBF) [42, 45]. During the fabrication of metal AM products, the deposited existing metal layer is reheated when the new layer is formed over the existing layers. The mechanical and morphological properties of metal AM products are changing due to reheating or IHT (Intercritical annealing, normalizing, and followed by long tempering process). The common classification of metal additive manufacturing methods is shown in Fig. 1. This review paper is fully focused on the effect of in-situ intrinsic heat treatment in WAAM, DED, and PBF products.

2.1 Wire Arc Additive Manufacturing (WAAM)

WAAM is a traditional additive manufacturing technique, the AM products are fabricated by welding technology. The part is formed, the new weld bead deposited over the existing weld bead through bead-by-bead technique [46]. A non-consumable electrode is used in gas tungsten arc welding (GTAW) [47] whereas a consumable electrode is used in Gas Metal Arc Welding (GMAW) [48]. Similarly, plasma energy is used in Plasma Arc Welding (PAW) [49]. Generally, the GTAW, GMAW and PAW techniques are commonly used in the WAAM process due to its higher metal deposition rate. The metal deposition rate of GMAW based additive manufacturing is two to three times higher than that of GTAW and PAW based additive manufacturing techniques [46]. In arc welding-based additive manufacturing technique, the deposition rate is controlled by a 3 axes or 6 axes automatic robotic arm [50]. However, some challenges in WAAM process such as welding defects [51], residual stress [52], distortion [53] and automation [54]. A movable gas nozzle provides CO_2, nitrogen, or argon gas as cooling medium in the WAAM process to fabricate the products during and/or after layer deposition (Fig. 2). The high arc energy produces the high temperature between electrode and the existing deposited weld bead. Both temperature and the heat cycle of the in-situ layer may be changed to create the required microstructure and mechanical properties [46].

2.2 Powder Bed Fusion

An alternative to conventional manufacturing techniques, PBF provides good dimensional control and the ability to create complex parts with high-resolution features [55]. It consists of an enclosed system, heat source (electron beam or laser), powder bed, powder feed to bed, scanner and an inert gas system [55]. The two most important factors impacting the effectiveness of this AM process are powder

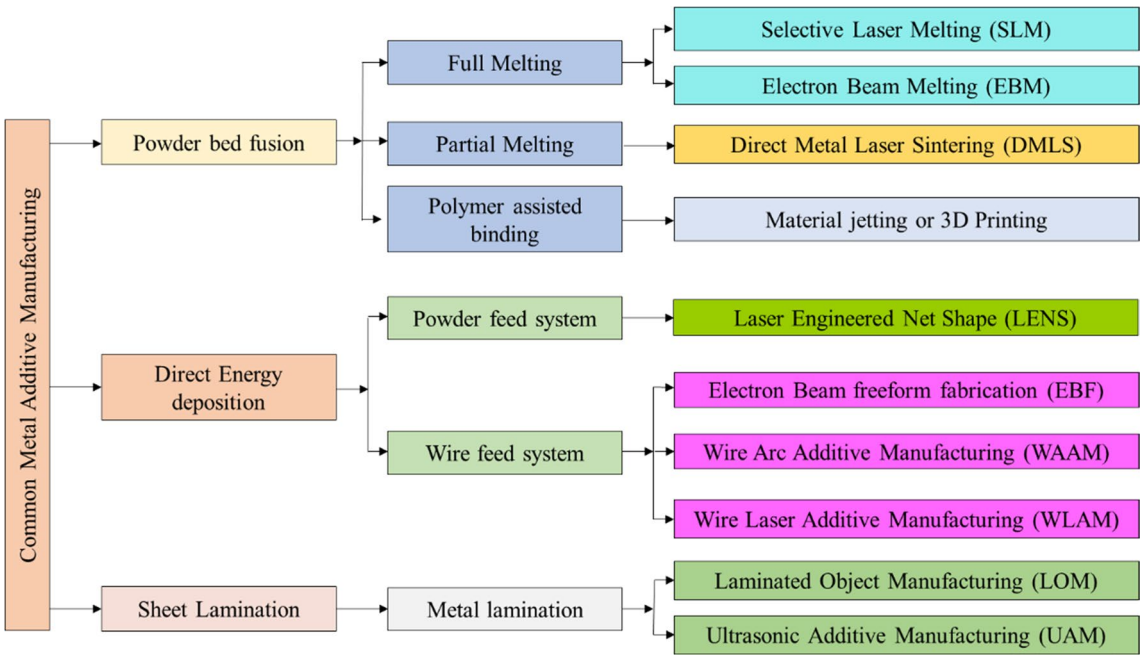

Fig. 1 Common types of metal additive manufacturing processes [34–37]

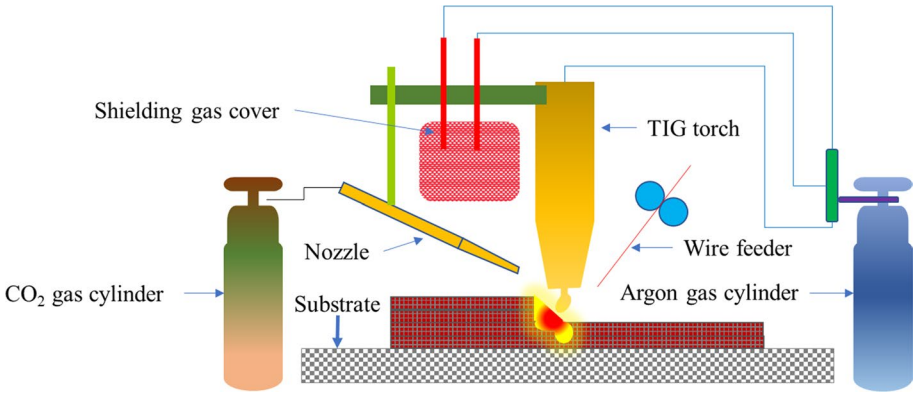

Fig. 2 Wire arc additive manufacturing setup with CO_2 cooling system [46]

size and particle density of the printed part [56]. According to the electron beam, PBF system is called as Electron Beam Melting (EBM) whereas based on the laser, it is known as Selective Laser Melting (SLM) [57]. The heat source (laser or electron beam), focusing mirror, or deflection coils are controlled the EBM and SLM processes to create the required properties of the products [55].

Figure 3a and b are examples of SLM and EBM systems, respectively. This type of powder bed formation system compacts a layer of powder particles between 20 and 60 microns in thickness by repeatedly raking or rolling metal powder from the metal source bed onto the build platform [60]. It reaches both thermal and mechanical stability required to build, which might have an impact on the printed part's performance [61]. The method is continued until the entire structure has been scanned at specific areas described by an uploaded CAD file [62]. The nearby unmelted powder of printed structure which acts as the mechanical support during the metal printing. After printing, the build chamber must be cleaned of surplus powder to extract the printed structure. The powder is removed and recycled immediately from EBM-created components. However, SLM procedures must first shift the powder to eliminate agglomeration during the printing process [61]. The primary drawbacks of PBF systems are their long processing times and high operating expenses [56].

2.3 Direct Energy Deposition (DED)

Direct Energy Deposition (DED) is a method of melting and fusing feed material as it is deposited on a substrate by utilizing concentrated thermal energy from a heat source [63–65]. It requires the post-processing due to lowers accuracy of the printed parts [60]. In contrast to PBF systems, DED printers can print huge amounts of parts and repair those broken by using them as substrates or building plates [55]. Figure 4a and b illustrate the powder feed and wire feed DED systems, respectively.

DED systems offer greater flexibility when it comes to heat sources and fuel sources. DED system, heat sources like lasers, arcs, and e-beams can be used whereas metal wires or powders can be used as feedstock material [61]. This method is also faster than PBF processing and allows the control of mechanical characteristics by controlling the chemical composition [35].

With subtractive manufacturing techniques such as a milling and drilling, DED systems may be utilized to make items with good surface finish and tolerances [56]. Due to their nature, these systems require additional maintenance to ensure component repeatability [61].

3 Heat Treatments in Additive Manufacturing

The solidification rates and several heating/cooling cycles of the metal additive manufacturing process are experienced similarly to traditional manufacturing technique like casting which could lead to significantly differing microstructure properties [67]. Heat treatments are required for wrought metal and welding process, same way it might also be required for AM components [68].

Titanium alloys undergo various phase transformations during thermal treatments, depending on the specific alloy composition and thermal processing conditions. Common phases in titanium alloys include α, β, α + β, and other phases such as martensite [69]. Heat treatments such as annealing, quenching, and aging can be used to modify the phase composition and microstructure of the material, leading to changes in mechanical and physical properties.

During hot isostatic pressing (HIP) of titanium alloy, the thermal history cycles involve heating the material to a high temperature and high pressure simultaneously, holding it at that temperature and pressure for a specific time to cause densification, and then cooling it at a controlled rate to prevent the formation of unwanted microstructures. After hot isostatic pressing (HIP), the microstructure of the Titanium

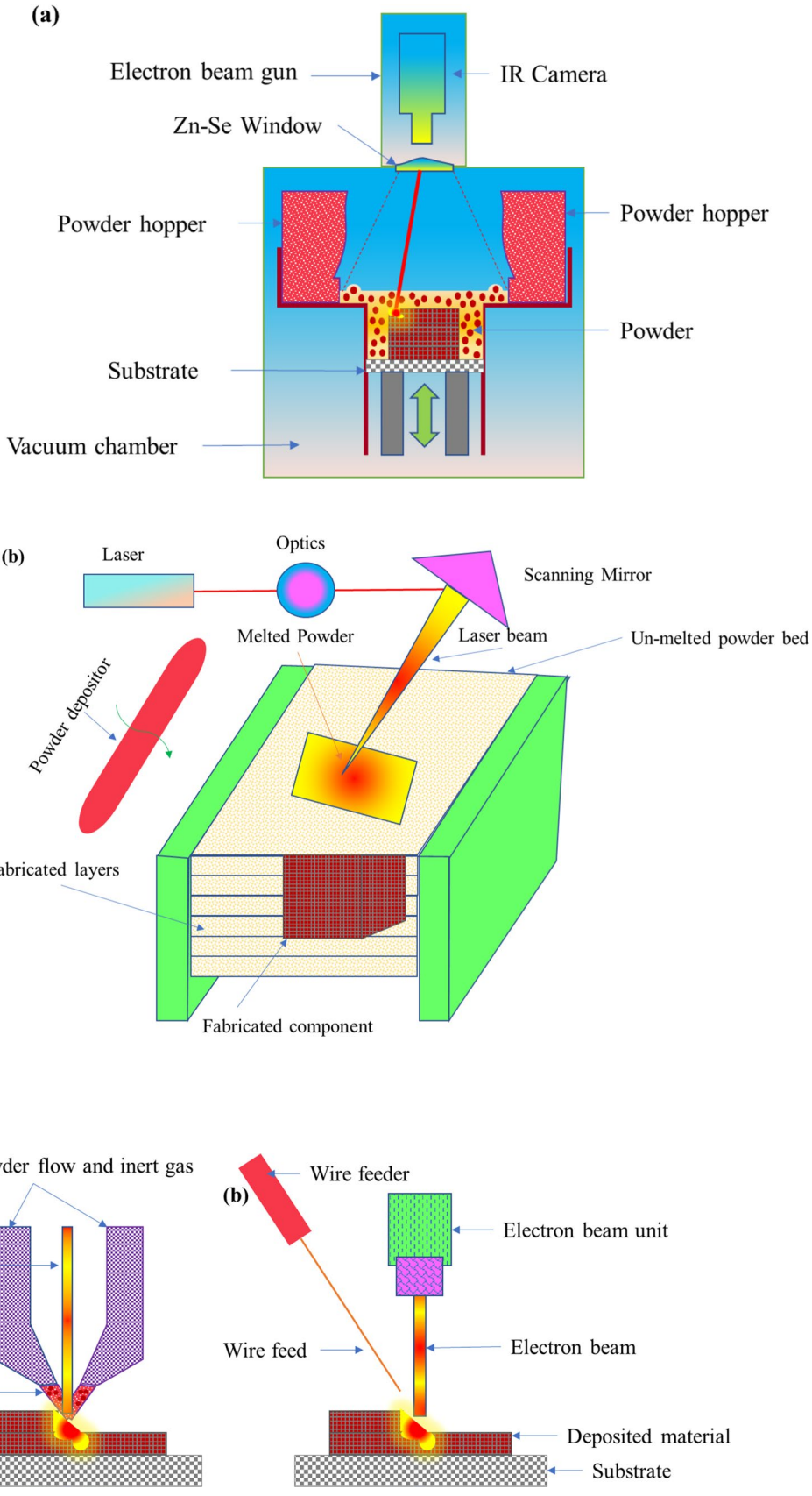

Fig. 3 Powder bed fusion setup **a** EBM [58] **b** SLM [59]

Fig. 4 DED setup **a** powder feed and laser-based DED **b** wire feed and electron-based DED system [66]

alloy appears as "nearly lamellar γ" (NL γ). During HIP, a decomposition reaction occurs within the α2/γ-colonies, whereby α transforms into β and γ. This reaction leads to an increase in the thickness of the γ-lamellae and the formation of secondary precipitates of the βo-phase within the α2/γ-colonies. The higher annealing temperature of 900 °C during the stabilization treatment caused the formation of γ-laths within the α2/γ-colonies and the onset of cellular reaction. For example, the α + β titanium alloy undergoes a phase transformation during cooling from the β-phase, with the α-phase precipitating out of the β-phase matrix. This transformation is time and temperature dependent and can be controlled by selecting specific cooling rates and aging temperatures [73].

The high cooling rates associated with metal additive manufacturing result in microstructures that are prone to microstructural inhomogeneities and defects, such as porosity, cracking, and residual stress. The IHT helps to mitigate these issues by controlling the cooling rate and providing the necessary thermal cycles to allow for the formation of homogeneous and fine-grained microstructures. The IHT can improve the mechanical properties of the material by reducing residual stress and improving the distribution of grain boundaries. This can result in a material with better fatigue resistance, tensile strength, and ductility. Therefore, the IHT is unavoidable in the design of additively manufactured metallic materials because it is necessary to mitigate the high cooling rates associated with the manufacturing process and to control the microstructure in order to improve the mechanical properties of the material [74].

The temperature profile of AM process is different from other convention processes during the layer upon layer technique. MAM and conventional manufacturing of Titanium alloys use the following post-heating treatments, such as hot isostatic pressing, high-temperature annealing, three-step annealing, and tempering as shown in Fig. 5 [71, 72]. The classification of common post heat treatments in additive manufacturing is shown in Fig. 6. Several researchers have claimed that annealing is the best heat treatment approach to remove residual stress. It makes it easier to produce high ductility for specific applications. An increase in annealing temperature reduces the UTS while breaking elongation rises, and its suggesting a considerable increase in ductile behavior [78]. Heat treatments, laser re-melting [79], shot peening [80] and hot isostatic pressing (HIP) [81] are some surface post heat treatment methods used to improve the performance of additive manufacturing components [82]. Vrancken et al. [83] employed heat treatments to improve the mechanical properties of SLM-Ti6Al4V. HIP is a post-heat-treatment process to repair process-related flaws in AM components and increase their fatigue performance [84, 85]. This review paper fully focuses on the effect of intrinsic heat treatment on the various additive manufacturing processes.

3.1 In-situ Intrinsic Heat Treatment in Metal Additive Manufacturing

Generally, Post heat treatments in MAM enhance the mechanical characteristics, reduce the residual stress, and modify the microstructure of materials. In Fig. 7, the feed material is deposited on the substate by the various heat sources such as welding ac, electron, and laser energy. The heat is accumulated on the existing layer while deposits new layer on the previous layer. It may be subjected to various thermal histories with respect to cooling medium, pause time and cooling duration. Intrinsic Heat Treatment (IHT) is defined as cyclic reheating [86], or the integration of multilevel Normalizing, multilevel annealing and followed by

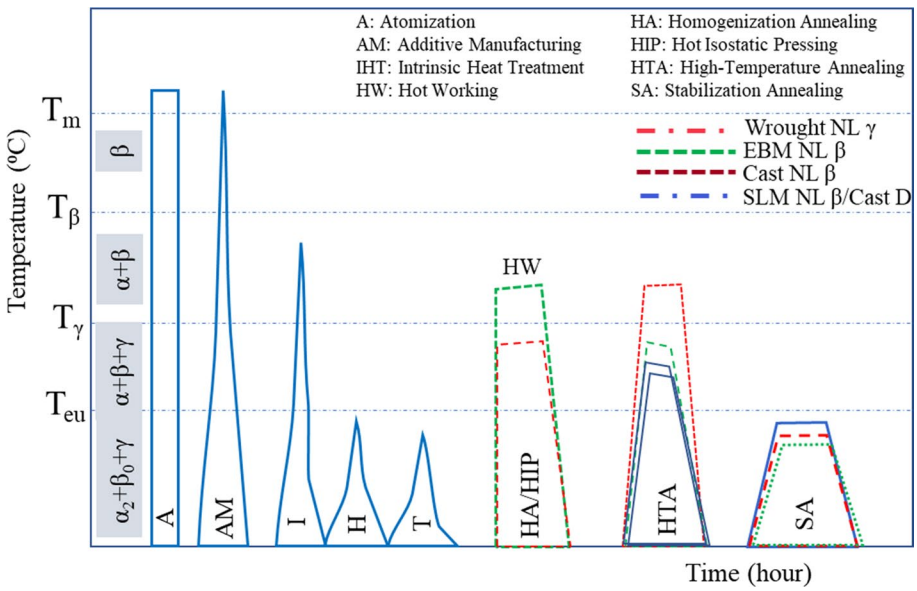

Fig. 5 Temperature history cycles of Titanium alloys for various HT processes [70–72]

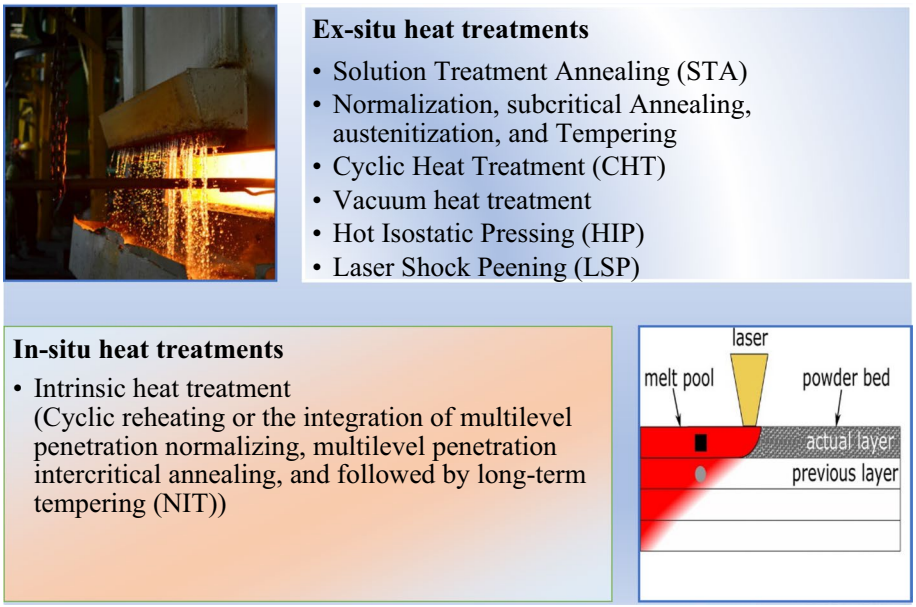

Fig. 6 Classification of common heat treatments in Metal Additive Manufacturing [75–77]

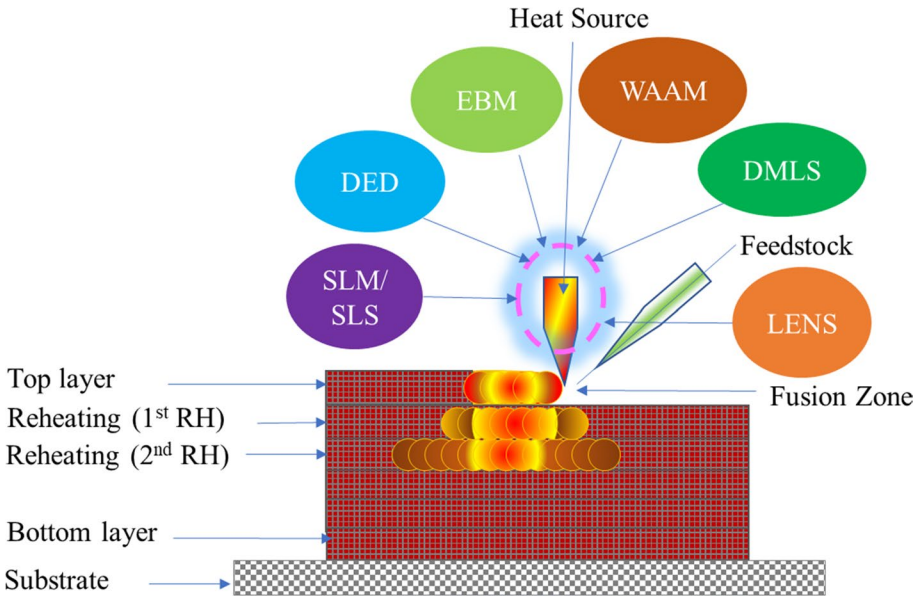

Fig. 7 Graphical representation of intrinsic heat treatment

long-term Tempering [87]. The welding and additive manufacturing techniques also produce similar thermal histories (Fig. 8), as indicated by the differences in microstructures [88]. The thermal heat cycles by the IHT, the material properties of AM products are improved without further post heat treatments.

Another example of thermal history cycles, Yuhang Li et al. [87] reported the example of a common temperature profile for SAAM low carbon steel, as shown in Fig. 9a. The temperature histories of five melt tracks are shown as solid red lines corresponding to the deposition of the 29th to 33rd layers (Fig. 9b). Inferred immeasurable heating cycles of layers near the fusion zone corresponding to passes 4 and 5 of the top four layers, were also used to highlight the influence of cyclic RHs on crystallization behavior (indicated by grey dotted lines).

In SAAM low carbon steel, the average temperature rate of 121 °C/s and peak temperature in pass 6 was 935 °C which was slightly more significant than 927 °C. When the temperature of the 3rd recorded peak (723 °C) did not surpass AC1, it was comparable to tempering. The temperature gradient became smaller as the heat source moved upward. As a result, the peaks of the various heat cycles were maintained comparably high levels for a longer duration. The material was normalized and inter-critical annealed during the entire tempering process.

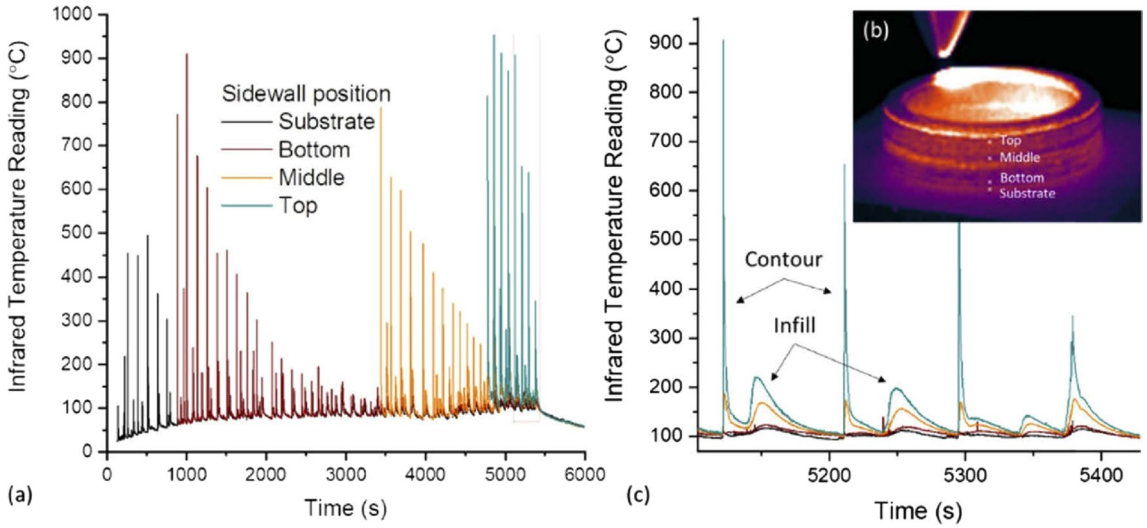

Fig. 8 Thermal history cycles for four regions in the AM sidewall [89]

During the first measured thermal cycle, the temperature above AC3 stayed steady for 5 s and remained in the dual-phase zone for 24 s (TC3's 6th RH, Fig. 9b). Multiple cycles of rapid austenitizing (normalizing) were eliminated by dynamic strain aging in C-Mn steel through a substantial refining impact on the microstructure [90, 91]. Hence, two layers below the fusing line were austenitized quickly during a single melt track (Fig. 9c).

Figure 10 depicts the microstructure evolution of the CGZ and HAZ that are affected by the series of melt tracks in layers 28–31. This evolution was derived from the thermal history recorded in thermocouples, which is represented by the red dotted line in Fig. 10a. This information could account for the presence of a homogenous microstructure dominated by equiaxial fine ferrite in the bulk of the SAAM component. When a 29th layer of molten metal is added on top of the 28th layer with a bead height of δ29, as seen in Fig. 10a, it is assumed that the local CGZ and CGHAZ of the 28th layer will be reheated to a temperature where the previous microstructure was fully γ-normalized but had not yet coarsened. This favorable condition results in the formation of uniform FGF and its dominance in the region affected by the temperature range of AC3-1100 °C. The 1st peak temperature of 935 °C obtained from TC3 falls within this range. As a result, most of the FGF in the 28th layer will be reheated to the inter-critical annealing range of AC1–AC3, leading to the decomposition of pearlite colonies into fine FGF and pearlite in the 29th layer when cooled from slightly expanded austenite. This creates a region with a predominant ferrite with a relatively uniform size, known as inter-critically reheated FGHAZ or ICFGHAZ, defined as PRF (partially refined ferrite).

However, when the previously deposited material is reheated below AC1 (tempering) by the 29th layer, no visible change in the FGF and PRF occurs. This stress-released PRF, called stress-released ferrite (SRF), dominates the local FGHAZ reheated to a temperature range of 500 ℃-AC1, known as sub-critically reheated FGHAZ (SCFGHAZ). The final microstructure of each sub-HAZ in the 29th layer will be affected by the subsequent 30th layer with a continuous temperature variation and a net bead height of δ30. The 2nd peak temperature of 780 °C at TC3 is slightly higher than AC1, indicating that the corresponding position in the 29th layer will be inter-critically annealed by the 30th layer. The final microstructure of the corresponding position in the 30th layer will be tempered to a temperature below AC1, forming an SRF-dominated microstructure [87] Table 1.

3.2 Low Carbon Steel

The total layers of the SAAM component from the substrate was 67 with each bead height being 1.43 mm. IHT revealed the SAAM component's morphology especially in the top 6th and 30th layers. The top layer was designated "no reheat (RH)," the preceding layer as "once RH," the antepenultimate layer as "double RH," and the 30th layer as the "37th RH" was appropriate. Slender grain boundary ferrite (GBF) and little polygonal ferrite (PF) dominated the microstructure in the top layer as a consequence of the feedstock, including a few acicular ferrites (AF) that promoted alloy elements (Fig. 11a) [99]. Additionally, widmanstatten ferrite was observed along grain boundaries of the previous austenitic phase. Due to poor heat dissipation, a minimal amount of residual matrix

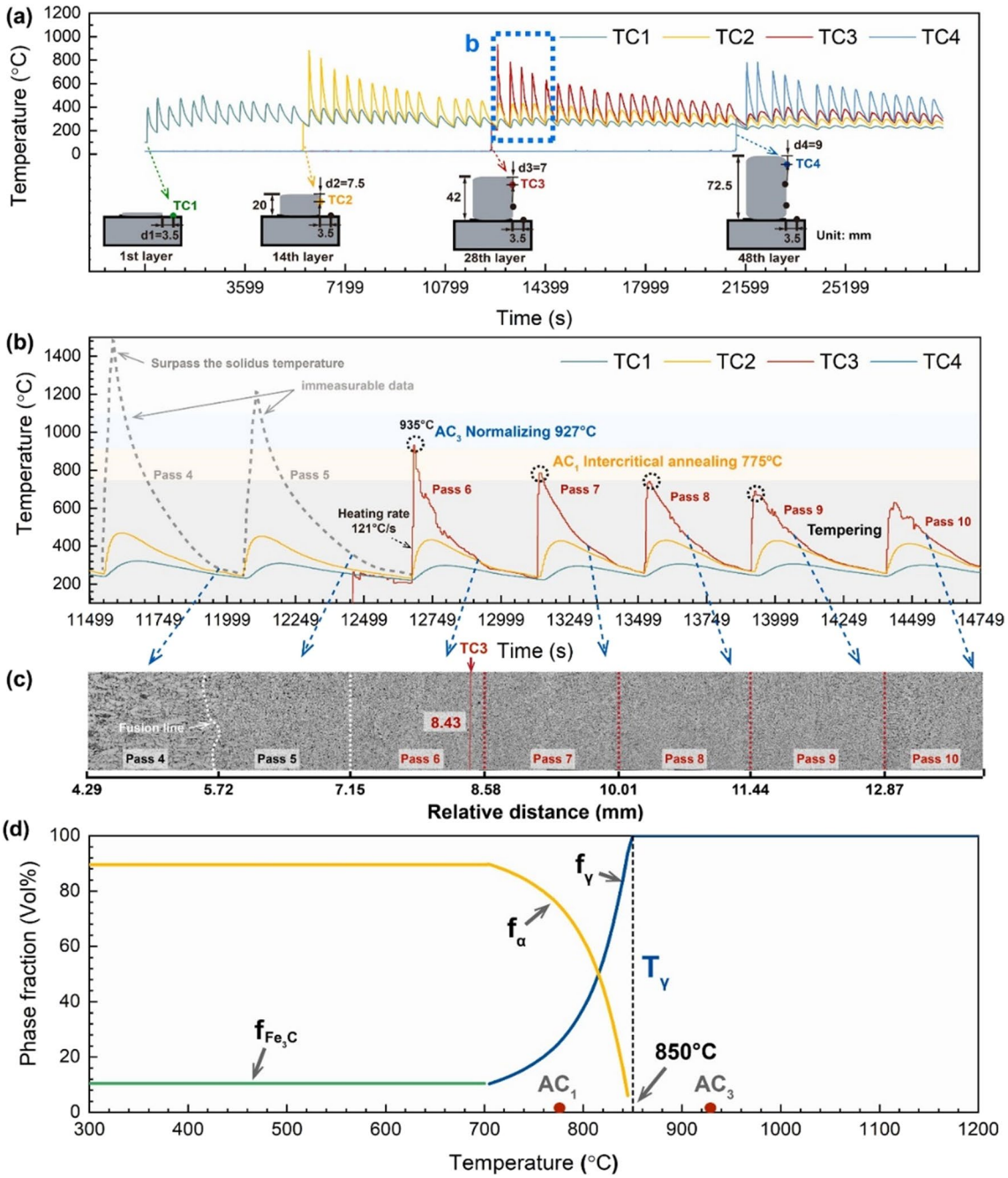

Fig. 9 Temperature history cycles measured by **a** thermocouple in 1, 14, 28, and 48th layer from the top of SAAM component **b** temperature history of 29 to 33rd layer **c** Optical microscopy for pass 4 to 10 (4.2 mm from top to 12.87 mm) (Reproduced with permission) [87]

was occupied by lamellar pearlite (LP) and AF. According to continuous cooling transformation, the low cooling rate of this low temperature facilitated the precipitation of brittle grain boundary ferrite and widmanstatten ferrite [63, 90]. Thus, the maximum size of ferrite was 46.8 µm as obtained in this region. (Fig. 11b). Brittleness of these coarse columnar granules are damaged the mechanical characteristics [100].

A coarse-grain heat-affected zone (CGHAZ) was formed by three RHs that transformed coarser columnar GBFs with the preceding structures being CGF (Fig. 11a). As a result of various allotropic changes in succeeding RHs, the coarse microstructures were reorganized and recrystallized (Fig. 11b). The homogenized zone was evenly distributed with equiaxial fine-grain ferrite (FGF) and highly scattered Lamellar Pearlite (LP) (Fig. 11a, e, f). The collapsed

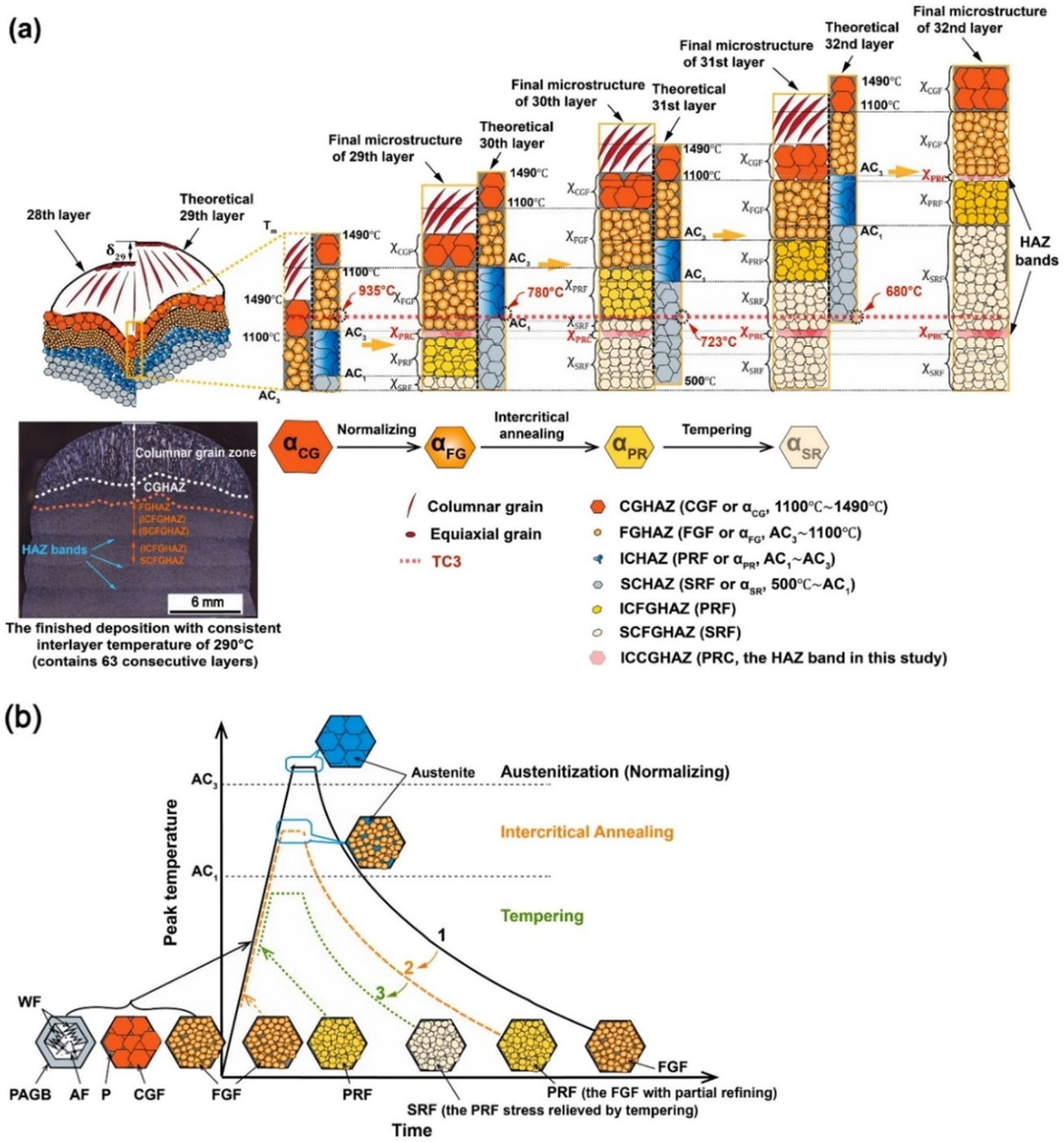

Fig. 10 **a** Microstructural evolution of low carbon steel due to the effect of IHT during SAAM **b** Phase changes in low carbon steel owing to IHT [87]. (Reproduced with permission)

lamellar lattice had cementite particles of 100–500 nm diameter (Fig. 11g). The ferrite matrix also contained nanosized cementite particles.

The random texture was derived from the strong texture in the CGZ (Figs. 12a and 13a). The influence of cyclic RHs on microstructural development and grain orientation change was investigated using EBSD measurements (Figs. 12 and 13). Columnar GBFs exhibited a characteristic < 001 > orientation on the inverse pole figures (IPF) at 4 mm from the top. Figure 11a, c shows the needle-like grains with AF that surround GBFs. As a result of cyclic RHs, the microstructure in the homogenized zone displayed a random orientation

Table 1 Effects of in-situ Intrinsic heat treatment on various materials

References	Fabrication methods	Materials	Methods to find the impact of in-situ IHT	Inference
Thomas Klein et al. [92]	WAAM	Al-Mg-Zn-Cu	SEM, WAXS, SAXS, Hardness test	The intrinsic heat treatment results in the formation of Mg-, Zn-, and Cu-rich phases at different length scales, ranging from 10 µm (micro segregations) to a few nm (bulk), as shown by these analyses due to IHT
Philipp Kürnsteiner et al. [93]	LMD	Maraging steel (Fe-19Ni-xAl)	EBSD, SEM, XRD, Vickers Hardness test	Studied the effect of varying Al content from 0 to 25% in Fe-19Ni-xAl steel by precipitates strengthening mechanism Atom probe tomography was used to find the intensity of nano-precipitates due to IHT
Sasan Amirabdollahian et al. [94]	DED	Maraging steel	SEM, Microhardness, Compressive test	Nanoprecipitation in maraging steel lead to increased yield strength and hardness. Thermal history cycles simulated by SIMUFACT Welding software and compared with actual values measured by thermocouples
James Damon et al. [95]	SLM	Low alloy steel (AISI 4140)	SEM, hardness test, Tensile test	Heat treatments such as quenching and tempering (Q&T) at 450 °C were considered for SLM IHT and compared to conventionally cast material Q&T
Andre Seidel et al. [70]	EBM	TiAl alloys	SEM	Lamellar spacing and lamellar grain structure were formed in γ-TiAl through reheating by adjusting laser power and temperature
Nan Kang et al. [96]	SLM	Commercial pure Ti (CP-Ti)	XRD, SEM, EBSD, and TEM	Sliding behaviors were carried out in three regions: surface, subsurface, and inner parts. Mechanical properties, microstructure, and tribological characteristics (Co-efficient of friction) were studied for AM CP Ti
Chaolin Tan et al. [97]	LAAM	AISI 420	SEM, EBSD, tensile test, compressive test	High amount of carbides were formed intrinsically due to the tempering effect High strength and ductility were obtained in AM 420SS due to the IHT effect Strengthening mechanism was done by twin boundary strengthening, grain boundary strengthening, dislocation strengthening, and precipitation strengthening

Table 1 (continued)

References	Fabrication methods	Materials	Methods to find the impact of in-situ IHT	Inference
Silja-Katharina Rittinghaus et al. [16]	L-DED	$AlCrFe_2Ni_2$		The face centered cubic phase fraction can be boosted to 58% with an intrinsic heat treatment that leads to the nucleation of new face centered cubic plates and thickening of existing ones. However, the heat affected zones at melt pool boundaries result in microstructural inhomogeneity that cannot be eliminated due to the brief interaction times
Philipp Kürnsteiner et al. [98]	DED	Fe19Ni5Ti	SEM, EBSD, Tensile test	As-built structure was composed of soft mesoscopic regions that lack nanoprecipitates and hard regions that contain a substantial amount of nanoscale precipitates. These precipitates were generated during the IHT process, which was initiated through the martensitic transformation that occurs during the cooling pause

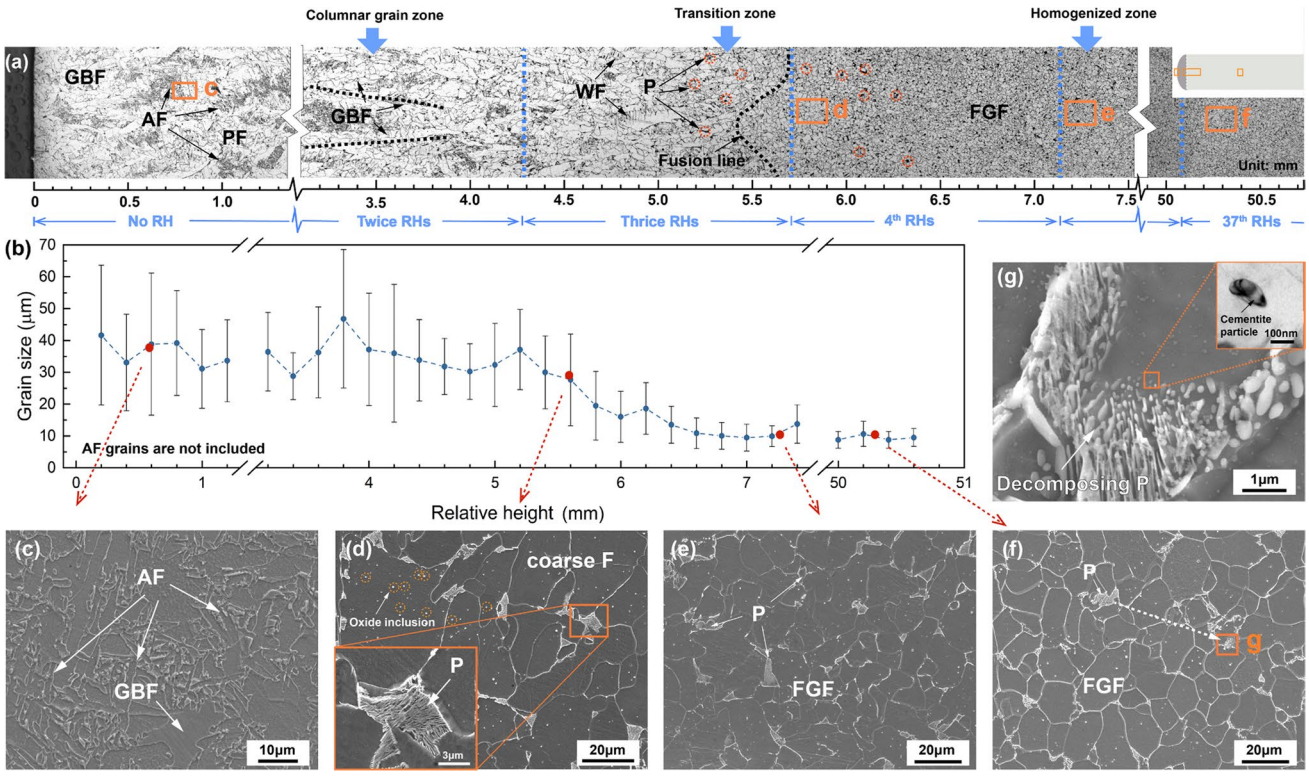

Fig. 11 **a** Optical microscopy-Microstructure change from top to 38th layer in the SAAM **b** grain size of SAAM component due to reheating **c**-**g** SEM magnified view from the top of 1, 5, 6, and 38th layer (Reproduced with permission) [87]

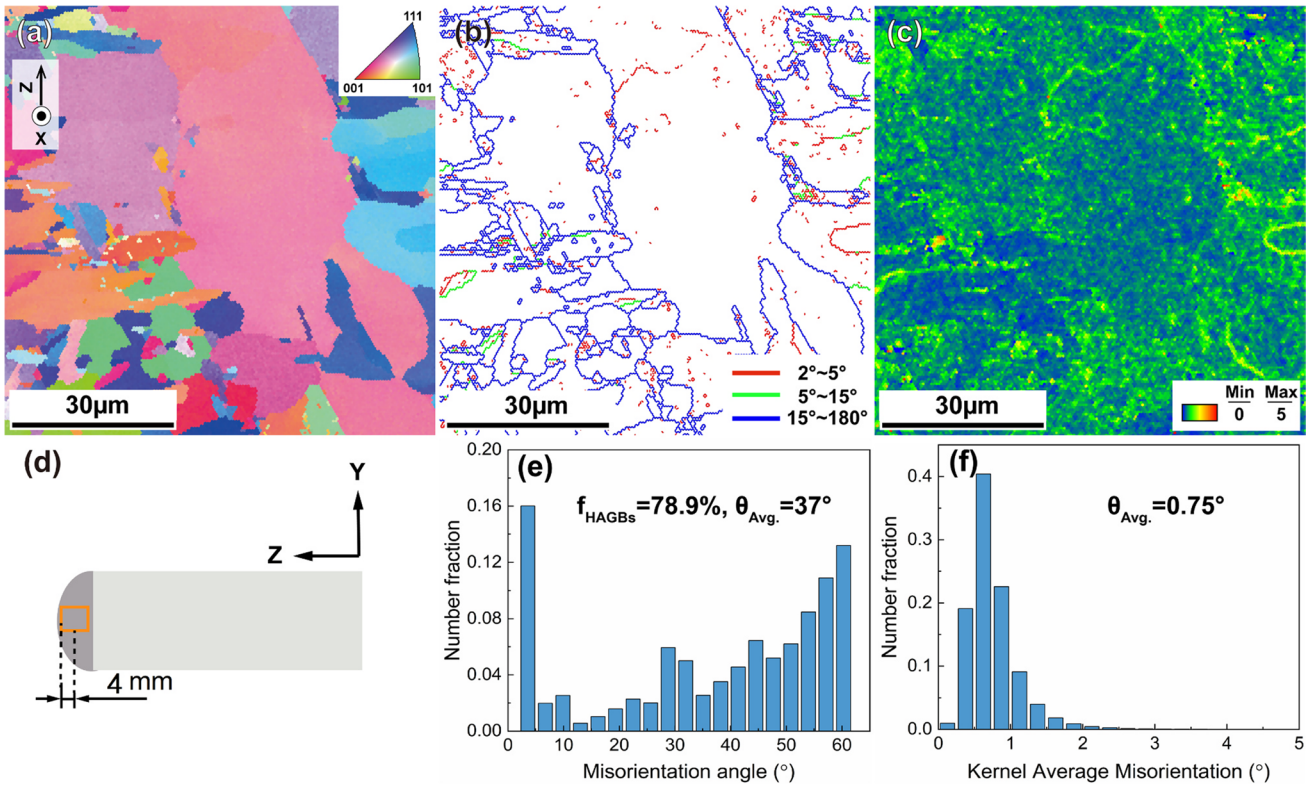

Fig. 12 EBSD analysis of SAAM component in the no reheat region (4 mm from the top) **a** IPF **b** misorientation map **c** kernel average misorientation map **d** graphical position representation for analysis **e** distribution of misorientation angle **f**distribution of KAM (Reproduced with permission) [87]

with expanded grain size (Fig. 11b), which exhibited a typical isotropic structure. Due to AF, a large portion of the CGZ was orientated between 40° and 60°.

In this study, the Kernel Average Misorientation (KAM) was used to explain the strain concentration at grain borders and to quantify the local strain level inside the grain. The greater the KAM value, the more severe the strain concentration and the greater the dislocation density, assuming that stored strain energy and dislocation density were nearly linear. Examining the strain levels in KAM maps of various SAAM sections helped understand cyclic RHs and their influence on microstructures. Compared to the homogenized zone, the CGZ had a smaller area proportion (83%) at 0–1°, as shown in Figs. 12c, f, and 13c, f. The homogenized zone microstructure showed a lower average KAM (0.60°) than coarse microstructures (0.75°). The geometrically necessary dislocation density and strain density were higher in the CGZ.

TEM images found the dislocations strongly clustered and tangled inside the CGZ (no RH) (Fig. 14a). The number of intracrystalline dislocations decreased considerably in the homogenized zone (36 times RH) (Fig. 14b). In this scenario, IHT might affect the crystal strain energy transitions and dislocations.

The mechanical properties of various materials due to IHT are listed in Table 2. Ultimate tensile strength and elongation of the SAAM low-carbon steel components was measured horizontally at 454 MPa and 29.8% and in the vertical direction at 441 MPa and 35.6%, respectively. The Vickers hardness of SAAM low carbon steel was approximately 148 HV [87].

3.3 Maraging Steel

Sasan Amirabdollahian et al. [94] discussed an excellent thermal history cycles by optimizing pause temperature due to the effect of IHT conditions for L-DED maraging steel. Three samples were fabricated, each having 15 layers, and three distinct pause periods between layers were used in the fabrication. Stop intervals for each layer were 30 s-P (Stop Pause Intervals), 120 s-P, and 250 s-P. Figure 15a–c show the thermal history simulations based on interlayer pauses in the 1st and 12th layers of the 15 subsequent layers.

The period for cooling during 30 s-P deposition (Fig. 15a) was inadequate to cool the first deposited layer below the martensite start temperature (Ms) (215 °C) indicating that the layer would never go through martensitic transformation.

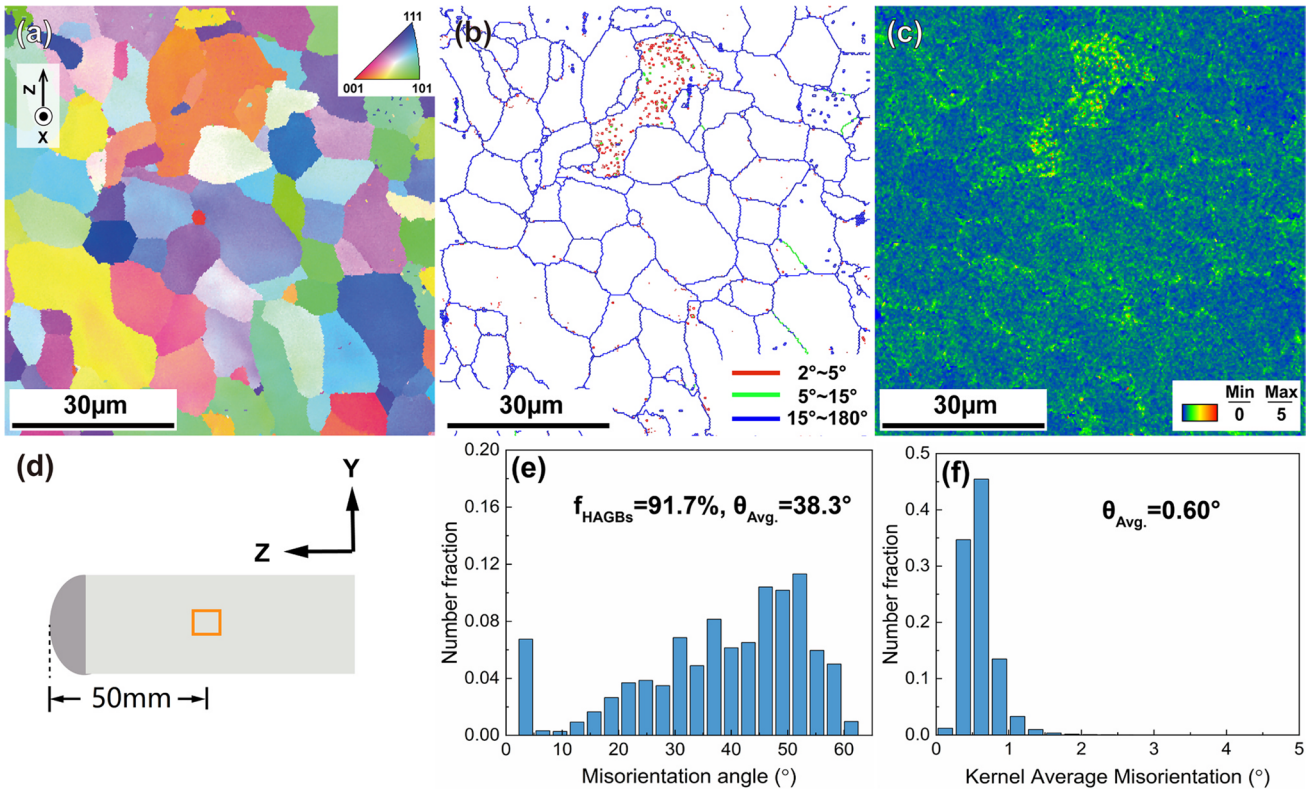

Fig. 13 EBSD analysis of SAAM component in the 37th reheating (50 mm from the top) **a** IPF **b** misorientation map **c** kernel average misorientation map **d** graphical position representation for analysis **e** distribution of misorientation angle **f** distribution of KAM (Reproduced with permission) [87]

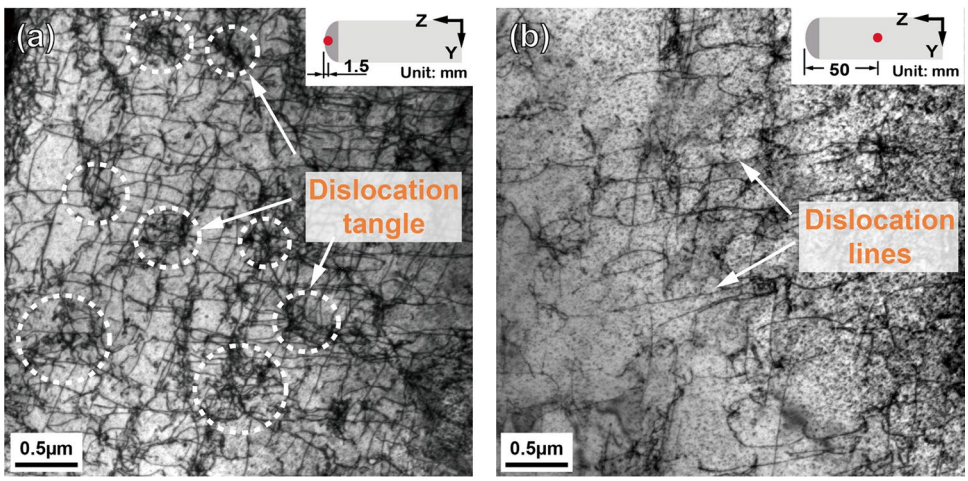

Fig. 14 Magnified SEM images **a** Dislocation in the top layer (1.5 mm from the top) **b** Dislocation in the 38th layer (50 mm from the top) (Reproduced with permission) [87]

In the first layer of the 120 s-P situation, martensite finish temperatures were above 100 °C (Fig. 15b). After cooling, the material fully transformed into martensitic. A thermal cycle occurred in the 1st layer and till the formation of the 6th layer above the α → γ transformation temperature. During the 120 s delay caused by the deposition of the 7th layer, temperature in the first layer increased to about 650 °C after cooling. Martensite was precipitated as intermetallic particles at this temperature. In this phase, the first layer was subjected to aging. The highest possible temperature in the last three layers was always more significant than the α → γ phase transition thereby preventing aging. Therefore, the top layers should not age.

During the subsequssent layer deposition in 250 s-P (Fig. 15c), the first deposited layer was heated above α → γ phase transformation and cooled to temperatures below

Table 2 Mechanical Properties of various materials due to IHT

References	Materials	Methods	Position/condition of the specimen	Mechanical properties
Yuhang Li et al. [87]	Low carbon steel (EM12K)	SAAM	Upper horizontal	Yield strength- 324 MPa UTS- 436 MPa Strain- 29.8%
			Lower horizontal	Yield strength- 335 MPa UTS- 454 MPa Strain- 24.9%
			Longitudinal	Yield strength- 339 MPa UTS- 441 MPa Strain- 35%
Philipp Kürnsteiner et al. [93]	Maraging steel (Fe-19Ni-xAl)	LMD	Lower bound (wt 0% Al)	Hardness -225 HV
			Lower bound (wt 12% Al)	Hardness- 525 HV
Sasan Amirabdollahian et al. [94]	Maraging steel	DED	Pause time 30 s-P	Compression test Yield strength- 990 MPa
			Pause time 120 s-P	Compression test Yield strength- 1410 MPa
			Pause time 120 s-P	Compression test Yield strength- 1545 MPa
James Damon et al. [95]	Low alloy steel (AISI 4140)	SLM	As-built	Yield strength- 1175 MPa UTS-1280 MPa
			SLM (Q&T at 450 °C) IHT	Yield strength- 1290 MPa UTS- 1325 MPa
			Conv. (Q&T at 450 °C)	Yield strength- 1245 MPa UTS- 1417 MPa
Nan Kang et al. [96]	Commercial pure Ti	SLM	Surface (0–50 µm)	Young's modulus (E) -120 MPa Co-efficient of friction- 0.18
			Subsurface (50–200 µm)	Young's modulus (E) -128 MPa Co-efficient of friction- 0.32
			Inner part (below 200 µm)	Young's modulus (E) -150 MPa Co-efficient of friction- 0.45

the martensite finish temperature (50 °C). When layer one achieved its aging temperature interval, it would have completed the sixth layer deposition. The aging process continued throughout the deposition process. During the 250 s-P, the bottom layers of maraging steel undergo the multiple reheating process. Temperature fluctuations for all three deposition situations were recorded using a thermocouple coupled to the base plate. The temperature history simulation of the bottom plate with thermocouple measurements for the 250 s-P sample is shown in Fig. 15d. There was a good agreement when the simulation and experimental measurements for 250 s-P were compared.

SEM micrographs of sample 30 s-P, no significant precipitation was observed within the matrix (Fig. 16a), but nanoprecipitations of intermetallic (Fig. 16b) was found in the martensitic matrix of sample 250 s-P. Two types of nano-precipitates, such as finer elongated ones shown by red arrows and coarser spheres shown by yellow arrows (Fig. 16b) were seen in sample 250 s-P.

According to the compressive test, the yield strength of the 250 s-P sample was 1545 MPa, whereas the yield strength of the 120P-s sample was 1410 MPa. The yield strength of the as-built material was 990 MPa, with no pause imposed. The implementation of an appropriate pause technique to induce substantial in-situ nano-precipitation increased the hardness and yield strength of the material [94].

From Table 2, The mechanical properties such as yield strength and ultimate strength of as-built WAAM low carbon steel at the bottom of layers was higher than the top of the layers due to the effect of IHT (Yuhang Li et al. [87]). Similar to the inner surface of SLM Ti part was higher Young's modulus than the surface part (top of layers) of the material due the metallic precipitates formed owing to effect of IHT (Nan Kang et al. [96]).

3.4 Aluminum Alloy

In order to evaluate the effectiveness of IHT, it is important to study the evolution of the microstructure as a function of aging time [101]. One way to do this is by performing azimuthal integration scattering experiments on the printed parts, which can provide information about the distribution of crystallographic orientations and the size

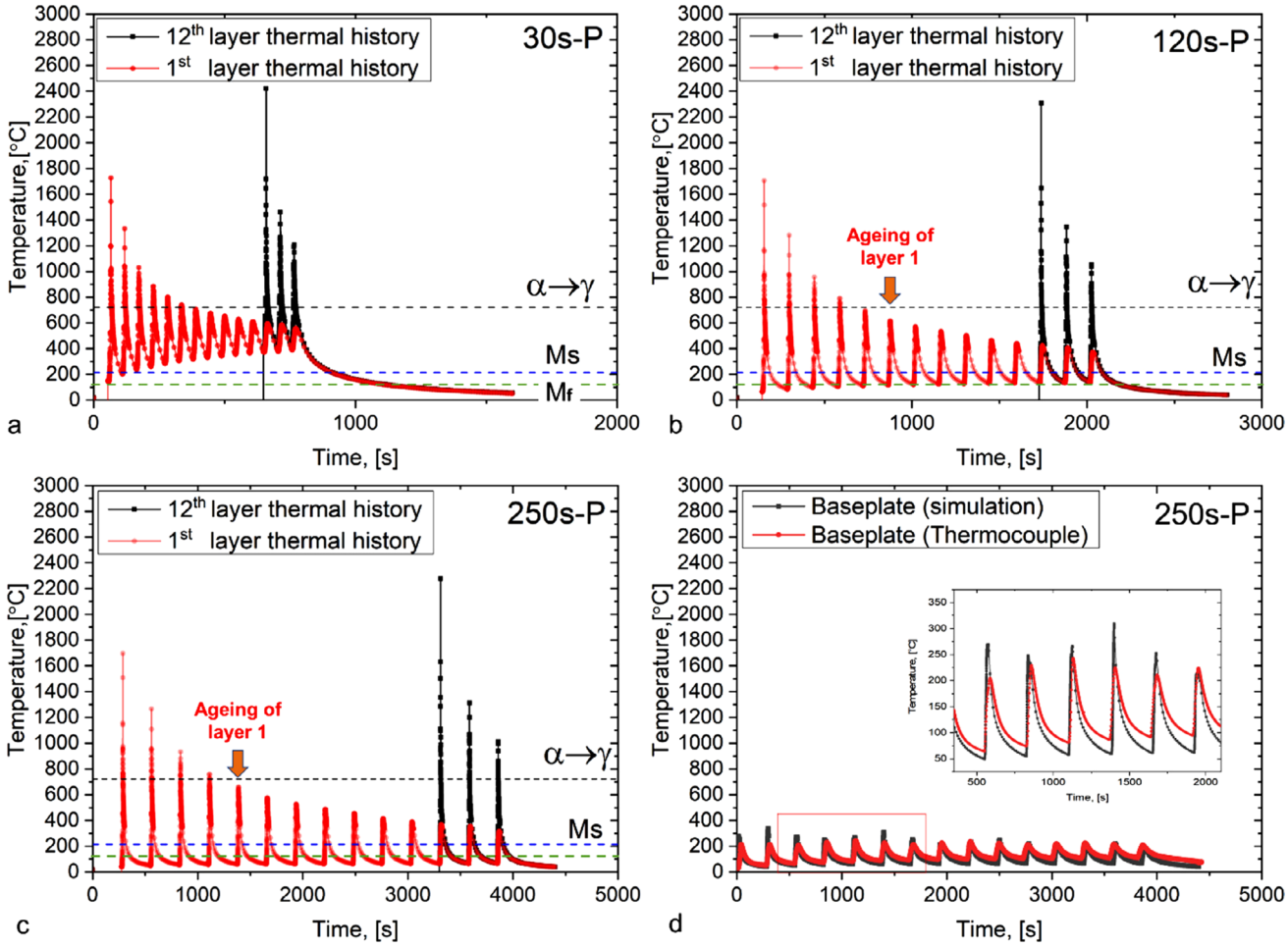

Fig. 15 Simulated thermal histories for deposited 1st and 12th layers **a** 30 s-P sample **b** 120 s-P sample **c** 250 s-P sample. **d** Temperature history of the bottom plate with thermocouple measurements and simulation results for the 250 s-P sample (Reproduced with permission) [94]

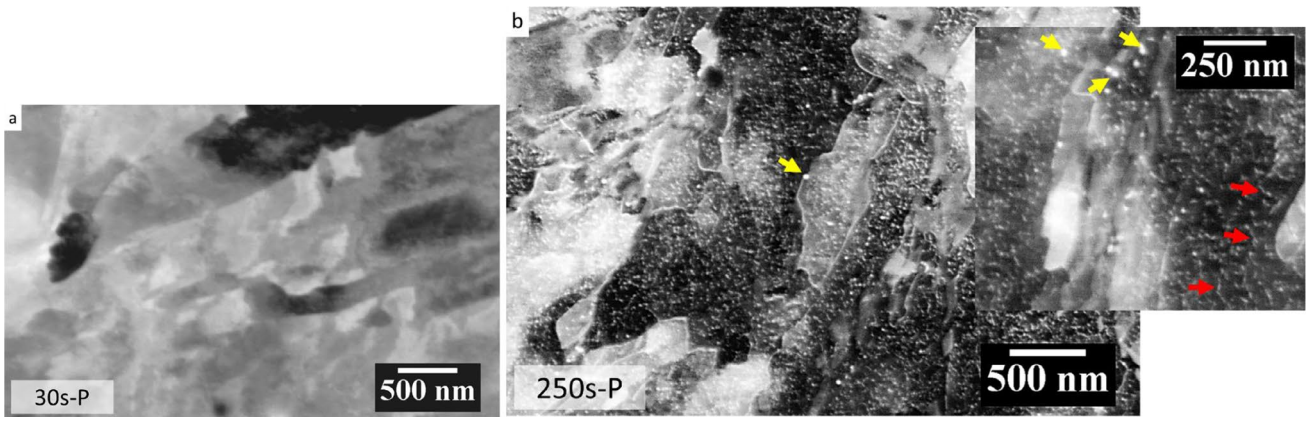

Fig. 16 SEM analysis **a** 30 s-P sample with martensitic microstructure, **b** 250 s-P sample with massive nanoprecipitation (Reproduced with permission) [94]

and shape of the grains. Figure 17 shows an overview of an in-situ synchrotron test on the Al–Mg-Zn-Cu alloy under IHT conditions. As aging time increased, the Wide-Angle X-ray Scattering (WAXS) signal indicated the increased diffraction peaks (T-phase) inside the α-Al structure [92, 102]. The diffraction peaks (T-phase) have been increased

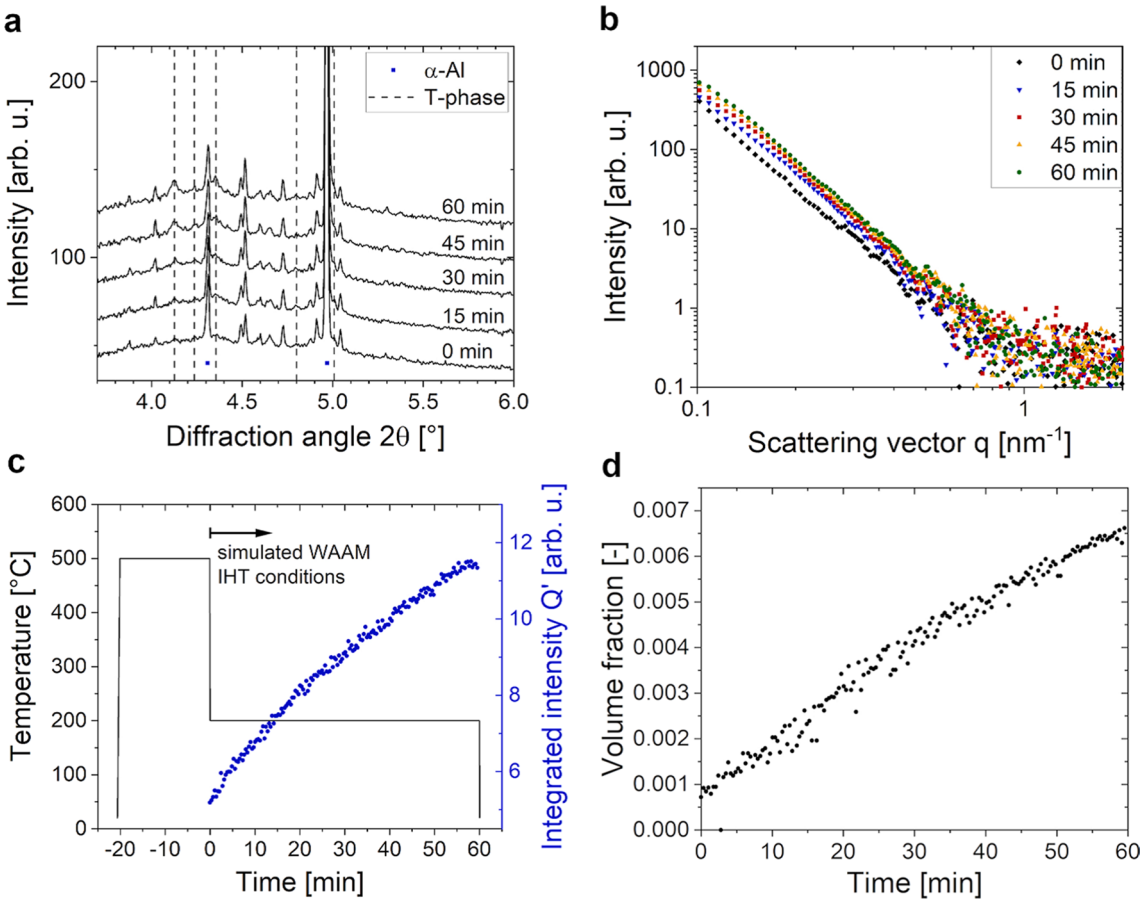

Fig. 17 Isothermal aging experiments during 60 min of diffraction and scattering **a** integrated intensity curves with diffraction angle '2θ' **b** Azimuthal integration scattering curves **c** Simulation of IHT and development of integrated intensity Q' during IHT **d** Fine precipitate volume fraction evolution (Reproduced with permission) [92]

at the diffraction angle of 5° for increasing aging time. The Small-Angle X-ray Scattering (SAXS) experiment results are depicted in Fig. 17b–d. Thomas Klein et al. [92] reported the formation of precipitates was accompanied by an increase in scattering intensity (Fig. 17b and c). Initially, the precipitates were less than 100 nm. Within the observed q range of the testing method, phases greater than 100 nm may only have an impact with an aq^{-4} gradient. The volume of fraction increased with increases the aging time. It was discovered that the particle fractions increased in the simulated IHT model. The results show that coarser phases were present after solidification and before the isothermal region [92].

The microhardness of the AM sample were 109 HV and 101 HV in the first and 20th layers respectively. It was predicted that alloying elements such as Mg and Zn in a solid solution influenced the hardness of the material at the topmost layer. IHT promoted the precipitation starting from the lowest layer. However, the precipitates had an unfavorable size distribution (Fig. 17d), indicating that material softening. There were no significant changes between grain interiors and grain boundaries in the WAAM of Aluminum 7075 alloy [28].

4 Conclusion

The source of heat is accumulated in the metal layers and then dissipated to the surroundings during the fabrication of MAM products due to multiple reheating during the deposit of the next layer over the existing layers. Hence, the material's mechanical properties, such as tensile strength, hardness, ductility, fatigue, etc., were enhanced through IHT while building the MAM component. In this study, built metal AM components had better mechanical properties than post-heat-treated AM components in many cases. The in-situ intrinsic heat treatment in MAM products has enhanced mechanical properties without any post-heat treatment in the build directions. Hence, it is suggested that the AM component's mechanical properties are enhanced by modifying the material's morphology through an appropriate pause time and holding time during the deposition of new layer.

Declarations

Conflict of interest The author declares that they have no conflict of interest.

References

1. L. Li, B. Post, V. Kunc, A.M. Elliott, M.P. Paranthaman, Scr. Mater. **135**, 100 (2017)
2. M. Oyesola, K. Mpofu, N. Mathe, Procedia Manuf. **35**, 155 (2019)
3. H. González, I. Arrizubieta, A. Calleja, J.E. Ruiz, A. Lamikiz, Procedia Manuf. **13**, 802 (2017)
4. A. Bacciaglia, A. Ceruti, A. Liverani, Procedia Comput. Sci. **200**, 1113 (2022)
5. R. Korsmik, I. Tsybulskiy, A. Rodionov, O. Klimova-Korsmik, M. Gogolukhina, S. Ivanov, G. Zadykyan, R. Mendagaliev, Procedia CIRP **94**, 298 (2020)
6. D. Herzog, V. Seyda, E. Wycisk, C. Emmelmann, Acta Mater. **117**, 371 (2016)
7. Y. Zhang, L. Wu, X. Guo, S. Kane, Y. Deng, Y.-G. Jung, J.-H. Lee, J. Zhang, J. Mater. Eng. Perform. **27**, 1 (2018)
8. N.A. Rosli, M.R. Alkahari, M.F. Abdollah, S. Maidin, F.R. Ramli, S.G. Herawan, J. Mater. Res. Technol. **11**, 2127 (2021)
9. C.R. Cunningham, J.M. Flynn, A. Shokrani, V. Dhokia, S.T. Newman, Addit. Manuf. **22**, 672 (2018)
10. J. Mazumder, A. Schifferer, J. Choi. **3**, 118 (1999)
11. L. Qian, J. Mei, J. Liang, X. Wu, **21**, 597 (2005)
12. W. Hofmeister, M. Griffith, JOM **53**, 30 (2001)
13. M. Zhao, C. Duan, X. Luo, **28**, 2225 (2022)
14. B. Zheng, Y. Zhou, J.E. Smugeresky, J.M. Schoenung, E.J. Lavernia, Metall. Mater. Trans. A **39**, 2228 (2008)
15. M.L. Griffith, M.E. Schlieriger, L.D. Harwell, M.S. Oliver, M.D. Baldwin, M.T. Ensz, M. Essien, J. Brooks, C.V. Robino, J.E. Smugeresky, W.H. Hofmeister, M.J. Wert, D.V. Nelson, Mater. Des. **20**, 107 (1999)
16. S.-K. Rittinghaus, A. Ali, U. Hecht, Met. Mater. Int. **29**, 579 (2023)
17. Y. Zhang, G. Yu, X. He, Sci. China Physics. Mech. Astron. **55**, 1431 (2012)
18. P. Krakhmalev, I. Yadroitsava, G. Fredriksson, I. Yadroitsev, Mater. Des. **87**, 380 (2015)
19. P. Dirisu, G. Supriyo, F. Martina, X. Xu, S. Williams, Int. J. Fatigue **130**, 105237 (2020)
20. V.R. Duarte, T.A. Rodrigues, N. Schell, R.M. Miranda, J.P. Oliveira, T.G. Santos, Addit. Manuf. **35**, 101193 (2020)
21. A. Ebrahimi, S. Kenny, M. Mohammadi, J. Offshore Mech. Arct. Eng. **143**, 011705 (2021)
22. L. Jiang, C. Chen, M. Zhang, Met. Mater. Int. **29**, 141 (2023)
23. W. Sha, Z. Guo, Precipitation hardening stainless steels, in *Maraging Steels* (Woodhead Publishing, Sawston, 2009), p. 141
24. R.F. Decker, *Source Book on Maraging Steels* (American Society for Metals, Metals Park, 1979)
25. J. Vishwakarma, K. Chattopadhyay, N.C. Santhi Srinivas, Mater. Sci. Eng. A **798**, 140130 (2020)
26. D. Raabe, D. Ponge, O. Dmitrieva, B. Sander, Adv. Eng. Mater. **11**, 547 (2009)
27. E.V. Pereloma, A. Shekhter, M.K. Miller, S.P. Ringer, Acta Mater. **52**, 5589 (2004)
28. B. Dong, X. Cai, S. Lin, X. Li, C. Fan, C. Yang, H. Sun, Addit. Manuf. **36**, 101447 (2020)
29. L.M.S. Santos, L.P. Borrego, J.A.M. Ferreira, J. de Jesus, J.D. Costa, C. Capela, Theor. Appl. Fract. Mech. **102**, 10 (2019)
30. T.H. Hsu, Y.J. Chang, C.Y. Huang, H.W. Yen, C.P. Chen, K.K. Jen, A.C. Yeh, J. Alloys Compd. **803**, 30 (2019)
31. H. Yves-Christian, W. Jan, M. Wilhelm, W. Konrad, P. Reinhart, Phys. Procedia **5**, 587 (2010)
32. P. Dong, F. Vecchiato, Z. Yang, P.A. Hooper, M.R. Wenman, Addit. Manuf. **40**, 101902 (2021)
33. N.T. Aboulkhair, I. Maskery, C. Tuck, I. Ashcroft, N.M. Everitt, Mater. Des. **104**, 174 (2016)
34. J.P.M. Pragana, R.F.V. Sampaio, I.M.F. Bragança, C.M.A. Silva, P.A.F. Martins, Adv. Ind. Manuf. Eng. **2**, 100032 (2021)
35. S. Cooke, K. Ahmadi, S. Willerth, R. Herring, J. Manuf. Process. **57**, 978 (2020)
36. A. Bandyopadhyay, Y. Zhang, S. Bose, Curr. Opin. Chem. Eng. **28**, 96 (2020)
37. P. Khanpara, S. Tanwar, Additive Manufacturing: Concepts and Technologies, in *A Roadmap to Industry 4.0: Smart Production, Sharp Business and Sustainable Development*. ed. by A. Nayyar, A. Kumar (Springer, Cham, 2020), pp. 171–185
38. J.C. Heigel, M.F. Gouge, P. Michaleris, T.A. Palmer, J. Mater. Process. Technol. **231**, 357 (2016)
39. D. Ding, Z. Pan, D. Cuiuri, H. Li, Int. J. Adv. Manuf. Technol. **81**, 465 (2015)
40. C. Li, Z.Y. Liu, X.Y. Fang, Y.B. Guo, Procedia CIRP **71**, 348 (2018)
41. J.C. Najmon, S. Raeisi, A. Tovar, Review of additive manufacturing technologies and applications in the aerospace industry, in *Additive Manufacturing for the Aerospace Industry*, ed. by F. Froes, R. Boyer (Elsevier, Amsterdam, 2019), pp. 7–31
42. M. Kumaran, V. Senthilkumar, Weld. World **65**, 1373 (2021)
43. V. Vinoth, T. Sekar, M. Kumaran, J. Mater. Eng. Perform. **32**, 4138 (2023)
44. P.M. Bhatt, A.M. Kabir, M. Peralta, H.A. Bruck, S.K. Gupta, Addit. Manuf. **27**, 278 (2019)
45. M. Kumaran, J. Mater. Eng. Perform. (2022). https://doi.org/10.1007/s11665-022-07513-w
46. B. Wu, Z. Pan, D. Ding, D. Cuiuri, H. Li, J. Xu, J. Norrish, J. Manuf. Process. **35**, 127 (2018)
47. H.-Y. Huang, Met. Mater. Int. **16**, 819 (2010)
48. P.G. Jönsson, R.C. Westhoff, J. Szekely, J. Appl. Phys. **74**, 5997 (1998)
49. A. Sahoo, S. Tripathy, Mater. Today Proc. **41**, 363 (2021)
50. S. Radel, A. Diourte, F. Soulié, O. Company, C. Bordreuil, Addit. Manuf. **26**, 106 (2019)
51. A. Horgar, H. Fostervoll, B. Nyhus, X. Ren, M. Eriksson, O.M. Akselsen, J. Mater. Process. Technol. **259**, 68 (2018)
52. S.R. Singh, P. Khanna, Mater. Today Proc. **44**, 118 (2021)
53. H. Huang, N. Ma, J. Chen, Z. Feng, H. Murakawa, Addit. Manuf. **34**, 101248 (2020)
54. C. Xia, Z. Pan, J. Polden, H. Li, Y. Xu, S. Chen, Y. Zhang, J. Manuf. Syst. **57**, 31 (2020)
55. W.E. Frazier, J. Mater. Eng. Perform. **23**, 1917 (2014)
56. T.D. Ngo, A. Kashani, G. Imbalzano, K.T.Q. Nguyen, D. Hui, Compos. Part B Eng. **143**, 172 (2018)
57. J.A. Gonzalez, J. Mireles, S.W. Stafford, M.A. Perez, C.A. Terrazas, R.B. Wicker, J. Mater. Process. Technol. **264**, 200 (2019)
58. A. Nouri, A. Sola, Electron beam melting in biomedical manufacturing, in *Metallic Biomaterials Processing and Medical Device Manufacturing*, ed. by C. Wen (Woodhead Publishing, Sawston, 2020), pp. 271–314
59. J. Gunasekaran, P. Sevvel, I.J. Solomon, Mater. Today Proc. **37**, 252 (2020)
60. T. Duda, L.V. Raghavan, IFAC-PapersOnLine **49**, 103 (2016)
61. W.J. Sames, F.A. List, S. Pannala, R.R. Dehoff, S.S. Babu, **61**, 315 (2016)

62. L.E. Murr, S.M. Gaytan, D.A. Ramirez, E. Martinez, J. Hernandez, K.N. Amato, P.W. Shindo, F.R. Medina, R.B. Wicker, J. Mater. Sci. Technol. **28**, 1 (2012)
63. M.E. Glicksman, *Principles of Solidification An Introduction to Modern Casting and Crystal Growth Concepts* (Springer, New York, 2011)
64. W. Choo, M. Ebrahimian, K. Choi, J.H. Kim, Met. Mater. Int. **29**, 1750 (2023)
65. K. Ha, Y.H. Moon, T.H. Kim, G.Y. Baek, K.Y. Lee, D.-S. Shim, W. Lee, Met. Mater. Int. **29**, 1399 (2023)
66. S.L. Sing, C.F. Tey, J.H.K. Tan, S. Huang, W.Y. Yeong, 3D printing of metals in rapid prototyping of biomaterials: Techniques in additive manufacturing, in *Rapid Prototyping of Biomaterials: Techniques in Additive Manufacturing*, 2nd edn., ed. by R. Narayan (Woodhead Publishing, Sawston, 2020), pp. 17–40
67. D. Zhang, S. Sun, D. Qiu, M.A. Gibson, M.S. Dargusch, M. Brandt, M. Qian, M. Easton, Adv. Eng. Mater. **20**, 1700952 (2018)
68. T.A. Rodrigues, J.D. Escobar, J. Shen, V.R. Duarte, G.G. Ribamar, J.A. Avila, E. Maawad, N. Schell, T.G. Santos, J.P. Oliveira, Addit. Manuf. **48**, 102428 (2021)
69. Y.L. Zhou, M. Niinomi, T. Akahori, Mater. Sci. Eng. A **384**, 92 (2004)
70. A. Seidel, S. Saha, T. Maiwald, J. Moritz, S. Polenz, A. Marquardt, J. Kaspar, T. Finaske, E. Lopez, F. Brueckner, C. Leyens, JOM **71**, 1513 (2019)
71. E. Schwaighofer, H. Clemens, S. Mayer, J. Lindemann, J. Klose, W. Smarsly, V. Güther, Intermetallics **44**, 128 (2014)
72. A. Seidel, A. Straubel, T. Finaske, T. Maiwald, S. Polenz, M. Albert, J. Näsström, A. Marquardt, M. Riede, E. Lopez, F. Brueckner, E. Beyer, C. Leyens, J. Laser Appl. **30**, 032301 (2018)
73. M. Kastenhuber, T. Klein, H. Clemens, S. Mayer, Intermetallics **97**, 27 (2018)
74. Z. Zhu, W. Li, Q.B. Nguyen, X. An, W. Lu, Z. Li, F.L. Ng, S.M. Ling Nai, J. Wei, Addit. Manuf. **35**, 101300 (2020)
75. M.J. Bermingham, L. Nicastro, D. Kent, Y. Chen, M.S. Dargusch, J. Alloys Compd. **753**, 247 (2018)
76. J. Chi, Z. Cai, Z. Wan, H. Zhang, Z. Chen, L. Li, Y. Li, P. Peng, W. Guo, Surf. Coat. Tech. **396**, 125908 (2020)
77. X. Yu, X. Lin, F. Liu, L. Wang, Y. Tang, J. Li, S. Zhang, W. Huang, Mater. Sci. Eng. A **798**, 140092 (2020)
78. A.K. Singla, M. Banerjee, A. Sharma, J. Singh, A. Bansal, M.K. Gupta, N. Khanna, A.S. Shahi, D.K. Goyal, J. Manuf. Process. **64**, 161 (2021)
79. E. Yasa, J. Deckers, J.P. Kruth, Rapid Prototyp. J. **17**, 312 (2011)
80. L. Hackel, J.R. Rankin, A. Rubenchik, W.E. King, M. Matthews, Addit. Manuf. **24**, 67 (2018)
81. A. du Plessis, E. Macdonald, Addit. Manuf. **34**, 101191 (2020)
82. B. AlMangour, J.M. Yang, Mater. Des. **110**, 914 (2016)
83. B. Vrancken, L. Thijs, J.P. Kruth, J. Van Humbeeck, J. Alloys Compd. **541**, 177 (2012)
84. A. Yadollahi, N. Shamsaei, Int. J. Fatigue **98**, 14 (2017)
85. K. Chadha, Y. Tian, J. Spray, C. Aranas, Met. Mater. Int. **28**, 237 (2022)
86. J. Zhang, Y. Liu, M. Bayat, Q. Tan, Y. Yin, Z. Fan, S. Liu, J.H. Hattel, M. Dargusch, M.X. Zhang, Scr. Mater. **191**, 155 (2021)
87. Y. Li, S. Wu, H. Li, Y. Dong, F. Cheng, Addit. Manuf. **46**, 102124 (2021)
88. T.A. Rodrigues, V. Duarte, J.A. Avila, T.G. Santos, R.M. Miranda, J.P. Oliveira, Addit. Manuf. **27**, 440 (2019)
89. J. Haley, C. Leach, B. Jordan, R. Dehoff, V. Paquit, Opt. Express **29**, 9927 (2021)
90. H. Bhadeshia, R. Honeycombe, *Steels: Microstructure and Properties*, 4th edn. (Butterworth-Heinemann, Oxford, 2017)
91. K. Liu, D. Wang, C. Deng, B. Gong, S. Wu, Mater. Sci. Eng. A **770**, 138541 (2020)
92. T. Klein, G. Graf, P. Staron, A. Stark, H. Clemens, P. Spoerk-Erdely, Mater. Lett. **303**, 130500 (2021)
93. P. Kürnsteiner, M.B. Wilms, A. Weisheit, P. Barriobero-Vila, E.A. Jägle, D. Raabe, Acta Mater. **129**, 52 (2017)
94. S. Amirabdollahian, F. Deirmina, L. Harris, R. Siriki, M. Pellizzari, P. Bosetti, A. Molinari, Scr. Mater. **201**, 113973 (2021)
95. J. Damon, R. Koch, D. Kaiser, G. Graf, S. Dietrich, V. Schulze, Addit. Manuf. **28**, 275 (2019)
96. N. Kang, N. Coniglio, Y. Cao, C. Zhao, M. El Mansori, Y. Zhao, X. Lin, C. Coddet, J. Tribol. **143**, 051102 (2021)
97. C. Tan, Y. Chew, F. Weng, S. Sui, Z. Du, F.L. Ng, G. Bi, Virtual Phys. Prototyp. **16**, 460 (2021)
98. P. Kürnsteiner, M.B. Wilms, A. Weisheit, B. Gault, E.A. Jägle, D. Raabe, Nature **582**, 515 (2020)
99. Y. Li, S. Wu, H. Li, F. Cheng, Mater. Lett. **283**, 128780 (2021)
100. H.E. Boyer, T.L. Gall, *Metals Handbook*, Desk edn. (American Society for Metals, Matals Park, 1985)
101. C. Tan, K. Zhou, W. Ma, P. Zhang, M. Liu, T. Kuang, Mater. Des. **134**, 23 (2017)
102. L. Stemper, B. Mitas, T. Kremmer, S. Otterbach, P.J. Uggowitzer, S. Pogatscher, Mater. Des. **181**, 107927 (2019)

Publisher's Note Springer Nature remains neutral with regard to jurisdictional claims in published maps and institutional affiliations.

Springer Nature or its licensor (e.g. a society or other partner) holds exclusive rights to this article under a publishing agreement with the author(s) or other rightsholder(s); author self-archiving of the accepted manuscript version of this article is solely governed by the terms of such publishing agreement and applicable law.